Probing negative-parity states of ^{24}Mg probed with proton and α inelastic scattering

Yoshiko Kanada-En'yo
Department of Physics, Kyoto University, Kyoto 606-8502, Japan

Kazuyuki Ogata
Research Center for Nuclear Physics (RCNP), Osaka University, Ibaraki 567-0047, Japan;
Department of Physics, Osaka City University, Osaka 558-8585, Japan;
and Nambu Yoichiro Institute of Theoretical and Experimental Physics (NITEP), Osaka City University, Osaka 558-8585, Japan

Background: The band structure of the negative-parity states of ^{24}Mg has not yet been clarified. The $K^{\pi} = 0^{-}$, $K^{\pi} = 1^{-}$, and $K^{\pi} = 3^{-}$ bands have been suggested, but the assignments have been inconsistent between experiments and theories.

Purpose: Negative-parity states of ^{24}Mg are investigated by microscopic structure and reaction calculations via proton and α inelastic scattering to clarify the band assignment for the observed negative-parity spectra.

Method: The structure of ^{24}Mg was calculated using the antisymmetrized molecular dynamics (AMD). Proton and α inelastic reactions were calculated using microscopic coupled-channel (MCC) calculations by folding the Melbourne g-matrix NN interaction with the AMD densities of ^{24}Mg.

Results: The member states of the $K^{\pi} = 0^{+}$, $K^{\pi} = 2^{+}$, $K^{\pi} = 0^{-}$, $K^{\pi} = 1^{-}$, and $K^{\pi} = 3^{-}$ bands of ^{24}Mg were obtained through the AMD result. In the MCC+AMD results for proton and α elastic and inelastic cross sections, reasonable agreements were obtained with existing data, except in the case of the 4_1^{+} state.

Conclusions: The 3^{-} state of the $K^{\pi} = 3^{-}$ band and the 1^{-} and 3^{-} states of the $K^{\pi} = 0^{-}$ bands were assigned to the 3_1^{-}(7.62 MeV), 1_1^{-}(7.56 MeV), and 3_2^{-}(8.36 MeV) states, respectively. The present AMD calculation is the first microscopic structure calculation to reproduce the energy ordering of the $K^{\pi} = 0^{-}$, $K^{\pi} = 1^{-}$, and $K^{\pi} = 3^{-}$ bands of ^{24}Mg.

I. INTRODUCTION

The band structure of ^{24}Mg has been studied via electromagnetic transitions [1–3], and intensively investigated through inelastic scattering of various probes, including electrons [4–10], pions [11], nucleons [12–23], ^{3}He [24,25], and α [25–29]. For inelastic hadron scattering off ^{24}Mg, detailed reaction analyses have been performed using the distorted-wave Born approximation (DWBA) and coupled-channel (CC) calculations. Reaction calculations using the phenomenological potentials of collective models have succeeded in describing the cross sections of low-lying positive-parity states in the $K^{\pi} = 0^{+}$ ground- and $K^{\pi} = 2^{+}$ sidebands (other than the 4_1^{+} state), and have also suggested deformations, including triaxial and hexadecapole shapes for ^{24}Mg.

For low-lying negative-parity states of ^{24}Mg, member states in the $K^{\pi} = 3^{-}$ and $K^{\pi} = 0^{-}$ bands and candidates for the $K^{\pi} = 1^{-}$ band have been reported by measurements of the γ decays [2], but the description of inelastic cross sections via reaction calculations has proven unsatisfactory, and the band assignments of negative-parity spectra have not yet been confirmed. In experiments with electron inelastic scattering, various behaviors of the form factors have been observed for two 3^{-} states: the 3_1^{-}(7.62

MeV) state of the $K^{\pi} = 3^{-}$ band and the 3_2^{-}(8.36 MeV) state of the $K^{\pi} = 0^{-}$ band [10]. A structure calculation using the open-shell random-phase approximation (RPA) has predicted two types of particle-hole excitations for the two 3^{-} states and qualitatively described only the first peak of the observed form factors, but not the second peak of the 3_2^{-}(8.36 MeV) state. For the bandhead 1_1^{-}(7.56 MeV) state of the $K^{\pi} = 0^{-}$ band and the 1_2^{-}(8.44 MeV) state of the $K^{\pi} = 1^{-}$ bands, no calculation has yet succeeded in describing either form factors or inelastic hadron scattering. Moreover, high-quality electron and hadron inelastic scattering data for the 1^{-} states have been limited in quantity because it is generally difficult to resolve the 1_1^{-}(7.56 MeV) and 1_2^{-}(8.44 MeV) states from the highly populated 3_1^{-}(7.62 MeV) and 3_2^{-}(8.36 MeV) spectra existing closely to the weak 1^{-} spectra in inelastic scattering.

Recently, the structure of the negative-parity states of ^{24}Mg has been investigated by microscopic calculations using quasiparticle RPA [30,31] and antisymmetrized molecular dynamics (AMD) [32,33]. These structural studies have predicted low-lying isoscalar dipole excitations in the $K^{\pi} = 0^{-}$ and $K^{\pi} = 1^{-}$ bands and discussed the importance of the triaxial deformation and cluster structures of ^{24}Mg for

negative-parity excitations. However, the predicted energy spectra of the negative-parity bands have been inconsistent with the experimental band assignment presented in Ref. [2], and the negative-parity band structure of ^{24}Mg remains an open problem.

In the present paper, we aim to investigate the structure of low-lying states of ^{24}Mg via analyses of inelastic electron, proton, and α scattering. Our main interest is in the low-lying 1^- and 3^- states of the negative-parity bands. In general, inelastic electron and high-energy proton scattering directly detects the transition densities of excitations from the ground state, whereas the α scattering can sensitively probe the transitions at the outer surface region of target nuclei rather than the interior region, because of the strong absorbing α-nucleus potentials. Moreover, low-energy proton and α scattering may contain information about in-band transitions via CC effects and can, in principle, be used as probes for the band assignment. As for the structural inputs of ^{24}Mg, the existing (e, e') data have shown a strong state dependence of the form factors indicating that simple collective models do not work in describing the transition densities of inelastic transitions. Furthermore, exotic deformations beyond axial symmetric-quadrupole deformation, cluster structures, and configuration mixing are expected to be important in the low-lying states, including the ground state of the ^{24}Mg system.

To achieve this aim, we apply the AMD method [34–37] for the structure calculation of ^{24}Mg and perform microscopic coupled-channel (MCC) calculations of proton and α scattering. In the MCC calculations, the diagonal and transition densities of the target nuclei obtained with microscopic structure models are utilized as inputs of the CC reaction calculations in microscopic folding models, wherein the nucleon-nucleus and α-nucleus potentials are constructed by folding the effective NN interactions. In our previous studies [38–43], we have applied the MCC calculations to proton and α scattering off various target nuclei in the p- and sd-shell regions using the AMD densities and the Melbourne g-matrix NN interaction [44]. We have presented successful results of the MCC+AMD approach for the (p, p') and (α, α') cross sections of various excited states.

In this paper, we first calculate the structure of ^{24}Mg with variation after parity and total-angular-momentum projections (VAP) in the AMD framework. The electromagnetic data (including transition strengths and electron scattering) are used to test the AMD result for the structural inputs. In particular, we compare the calculated transition strengths and form factors with the experimental data to check the assignment of predicted states to the experimental energy levels. To use the reaction calculations, we renormalize the AMD transition density to fit the electric-transition strengths, so as to reduce the model ambiguity of the structural inputs. We then apply the MCC approach to proton and α scattering off ^{24}Mg with the Melbourne g-matrix NN interaction using the AMD densities of ^{24}Mg. By analyzing these structure and reaction calculations, we can investigate the structure and transition properties of the ground ($K^\pi = 0^+$), $K^\pi = 2^+$, $K^\pi = 3^-$, $K^\pi = 0^-$, and $K^\pi = 1^-$ bands.

The rest of this study is organized as follows. In Sec. II, the frameworks for the AMD calculation for ^{24}Mg and for the MCC approach to proton and α scattering off ^{24}Mg are explained. The AMD results for the structural properties are described in Sec. III, while Sec. IV presents the proton- and α-scattering results. Finally, a summary is given in Sec. V.

II. METHOD

For the structure calculation of ^{24}Mg, we apply a VAP version of AMD, which is sometimes called AMD+VAP (though we use the name AMD in the present paper). This method has been applied for structural studies of various nuclei including ^{12}C and neutron-rich Be isotopes [36,45,46], and has also been used in the MCC+AMD calculation for reaction studies of proton and α scattering in Refs. [38–42]. The calculational procedures of the present structure and reaction calculations are almost the same as the MCC+AMD calculation for ^{20}Ne in Ref. [42]. For details, the reader is referred to those papers and the references contained therein.

A. AMD calculations for ^{24}Mg

In the AMD framework, an A-nucleon wave function is expressed by the Slater determinant of single-nucleon Gaussian wave functions as

$$\Phi_{\text{AMD}}(\mathbf{Z}) = \frac{1}{\sqrt{A!}} \mathcal{A}\{\varphi_1, \varphi_2, ..., \varphi_A\}, \tag{1}$$

$$\varphi_i = \phi_{\mathbf{X}_i} \chi_i \tau_i, \tag{2}$$

$$\phi_{\mathbf{X}_i}(\mathbf{r}_j) = \left(\frac{2\nu}{\pi}\right)^{3/4} \exp[-\nu(\mathbf{r}_j - \mathbf{X}_i)^2], \tag{3}$$

$$\chi_i = \left(\frac{1}{2} + \xi_i\right)\chi_\uparrow + \left(\frac{1}{2} - \xi_i\right)\chi_\downarrow. \tag{4}$$

Here, $\mathcal{A}$ is the antisymmetrizer, and φ_i is the ith single-particle wave function, written as a product of the spatial ($\phi_{\mathbf{X}_i}$), spin (χ_i), and isospin (τ_i) wave functions, where τ_i is fixed to be a proton or a neutron. The ν value of the width parameter is common for all single-nucleon Gaussians and is chosen to be $\nu = 0.16\,\text{fm}^{-2}$, which reproduces the root-mean-square radius of ^{16}O in the harmonic oscillator p-shell closed configuration. Parameters $\mathbf{Z} \equiv \{\mathbf{X}_1, ..., \mathbf{X}_A, \xi_1, ..., \xi_A\}$ (representing the Gaussian centroid positions and nucleon-spin orientations of the single-particle wave functions) are treated as variational parameters and determined by the energy optimization for each J^π state of ^{24}Mg. Energy variation is performed after the parity and total-angular-momentum projections so as to minimize the energy expectation value $E = \langle\Psi|\hat{H}|\Psi\rangle/\langle\Psi|\Psi\rangle$ for $\Psi = P^{J\pi}_{MM'}\Phi_{\text{AMD}}(\mathbf{Z})$ as projected from the AMD wave function with the parity and total-angular-momentum projection operator $P^{J\pi}_{MM'}$.

The VAP is performed for $(J^\pi, M') = (0^+, 0)$, $(2^+, 0)$, $(3^+, 2)$, and $(4^+, 0)$ to obtain the member states of the $K^\pi = 0^+$ and $K^\pi = 2^+$ bands. For negative-parity states, VAPs are performed using $(J^\pi, M') = (1^-, 0)$, $(2^-, 1)$, $(3^-, 0)$, $(3^-, 3)$, $(4^-, 3)$, and $(5^-, 0)$, and the member states of the $K^\pi = 3^-$, $K^\pi = 0^-$, and $K^\pi = 1^-$ bands are obtained. Here M' is the quanta of

the Z component J_Z of the total-angular-momentum in the body-fixed frame but does not necessarily indicate the K quanta defined for the principal axis of the intrinsic state, because there is no constraint upon the orientation of the intrinsic deformation in the energy variation. This means that the principal axis of the intrinsic deformation can, in principle, be tilted from the Z axis. Indeed, VAP calculations with $(J^\pi, M') = (3^-, 0), (3^-, 3), (4^-, 3),$ and $(5^-, 0)$ yield the dominant configurations for the $K^\pi = 3^-$ band, whereas, in VAP calculations with $(J^\pi, M') = (1^-, 0)$, two kinds of configurations corresponding to the $K^\pi = 0^-$ and $K^\pi = 1^-$ bands are obtained as local minima.

After the VAP calculations, we obtain the optimized sets, $\mathbf{Z}^{(m)}$, for the intrinsic configurations $\Phi_{\text{AMD}}(\mathbf{Z}^{(m)})$, which are labeled by m for each parity as $m = 1, \ldots, 4$ for the positive-parity states and $m = 1, \ldots, 7$ for the negative-parity states. To obtain the final wave functions for the J^π states of ^{24}Mg, the obtained configurations are superposed by diagonalizing the Hamiltonian and norm matrices using the basis wave functions $P_{MM'}^{J^\pi}\Phi_{\text{AMD}}(\mathbf{Z}^{(m)})$, as projected from the obtained configurations. Such diagonalization is performed for M' and m, which correspond to K-mixing and configuration (m) mixing, respectively.

The effective nuclear interactions used in the present AMD calculation are the same as those in Refs. [36,38–41]; they are the MV1 (case 1) central force [47] with the parameters $(b, h, m) = (0, 0, 0.62)$ and the spin-orbit term of the G3RS force [48,49] with strength parameters $u_I = -u_{II} = 3000$ MeV. The Coulomb force is also included.

B. MCC calculation of proton and α scattering off ^{24}Mg

The elastic and inelastic cross sections of proton and α scattering off ^{24}Mg are calculated via MCC+AMD. The nucleon-nucleus potentials are constructed in a microscopic folding model, in which the diagonal and coupling potentials are calculated by folding the Melbourne g-matrix NN interaction [44] with the AMD diagonal and transition densities of ^{24}Mg. We adopt a simplified single-folding model described in Ref. [50]. We employ the Brieva and Rook (BR) prescription [51–53] to localize the exchange terms. The validity of the BR localization has been confirmed in Refs. [50,54,55], and this simplified single-folding model has been successfully applied to nucleon-nucleus elastic scattering for various cases [50,56–58]. The α-nucleus potentials are obtained by folding the calculated nucleon-nucleus potentials with an α density in an extended nucleon-nucleus folding (NAF) model [59].

The Melbourne g matrix is an effective NN interaction derived from a bare NN interaction of the Bonn B potential [60]. It contains energy and density dependencies with no adjustable parameter, and can be well applied to a systematic description of elastic and inelastic proton scattering off various nuclei at energies of $E_p = 40$–300 MeV [40–42,44,50,56,58] and also of elastic and inelastic α scattering at energies of $E_\alpha = 100$–400 MeV [38,39,41,42,59,61]. In the present reaction calculation, the spin-orbit term of the proton-nucleus potential is not account for to avoid complexity, as in Refs. [40,41].

	exp	AMD	
J^π (band)	E_x (MeV)	E_x (MeV)	R_m (fm)
$0_1^+(K^\pi = 0^+)$	0.00	0.0	3.02
$2_1^+(K^\pi = 0^+)$	1.37	0.9	3.02
$4_1^+(K^\pi = 0^+)$	4.12	3.3	3.01
$2_2^+(K^\pi = 2^+)$	4.24	8.1	3.06
$3_1^+(K^\pi = 2^+)$	5.24	8.8	3.06
$4_2^+(K^\pi = 2^+)$	6.01	9.6	3.05
$3_1^-(K^\pi = 3^-)$	7.62	11.7	3.02
$4^-(K^\pi = 3^-)$	9.30	13.5	3.02
$5^-(K^\pi = 3^-)$	11.59	15.4	3.02
$1_1^-(K^\pi = 0^-)$	7.56	13.2	3.12
$3_2^-(K^\pi = 0^-)$	8.36	14.2	3.11
$5^-(K^\pi = 0^-)$	10.03	15.6	3.08
$1_2^-(K^\pi = 1^-)$	8.44	14.2	3.10
$2_1^-(K^\pi = 1^-)$	8.86	14.5	3.10
$3^-(K^\pi = 1^-)$	10.33	15.2	3.10
$4^-(K^\pi = 1^-)$		15.5	3.09
$5^-(K^\pi = 1^-)$	13.06	17.9	3.09
	Q ($e$fm^2)	Q ($e$fm^2)	
$2^+ K^\pi = 0^+$	−16.6(6)	−15.1	

As structure inputs for the target nucleus, the diagonal [$\rho(r)$] and transition [$\rho^{\text{tr}}(r)$] densities of ^{24}Mg, as obtained by the AMD calculation, are used. To reduce the model ambiguity from the structure calculation, the theoretical-transition densities obtained by the AMD calculation are renormalized by the factor f^{tr} as $\rho^{\text{tr}}(r) \rightarrow f^{\text{tr}}\rho^{\text{tr}}(r)$ to fit the electromagnetic transition strengths or (e, e') data. If there are no data concerning the transition strength, the original AMD transition densities are used without renormalization.

The $J^\pi = 0_1^+, 1_{1,2}^-, 2_1^+, 3_{1,2,3}^-$, and $4_{1,2}^+$ states of ^{24}Mg, and all $\lambda \leqslant 4$ transitions between them are included in the CC calculation. For the excitation energies of ^{24}Mg, experimental values are adopted.

III. STRUCTURE OF ^{24}Mg

A. Band structure of ^{24}Mg

The AMD results of excitation energies (E_x) for the $K^\pi = 0^+$, $K^\pi = 2^+$, $K^\pi = 3^-$, $K^\pi = 0^-$, and $K^\pi = 1^-$ bands of ^{24}Mg are listed in Table I, together with the experimental data. The theoretical states, $\{0_1^+, 2_1^+, 4_1^+\}, \{2_2^+, 3_1^+, 4_2^+\}, \{3_1^-, 4_1^-, 5_1^-\}, \{1_1^-, 3_2^-, 5_2^-\},$ and $\{1_2^-, 2_1^-, 3_3^-, 4_2^-, 5_3^-\}$, are assigned to the $K^\pi = 0^+$, $K^\pi = 2^+$, $K^\pi = 3^-$, $K^\pi = 0^-$, and

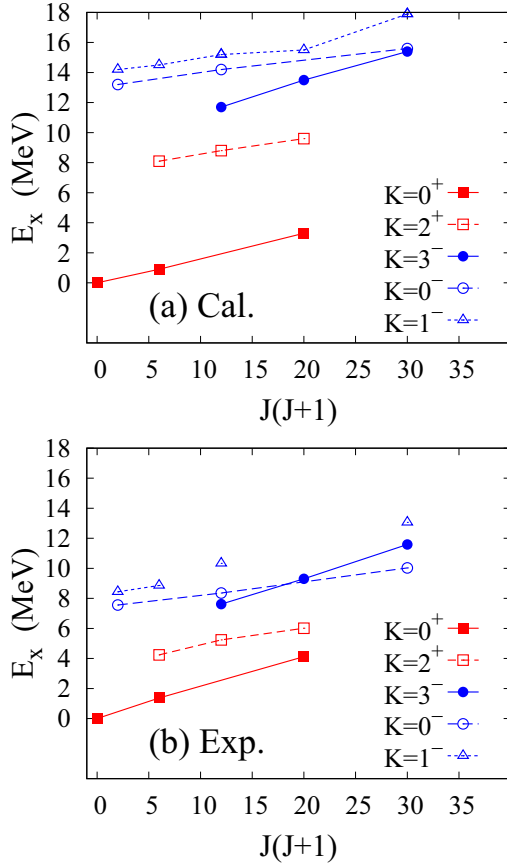FIG. 1. The energy spectra of ^{24}Mg. (a) The calculated energy levels. (b) The experimental levels for the $K^\pi = 2^+$ ground and the $K^\pi = 2^+$ sidebands from Ref. [62], and those for the $K^\pi = 3^-$, $K^\pi = 0^-$, and $K^\pi = 1^-$ bands assigned in Ref. [2].

$K^\pi = 1^-$ bands based upon analysis of the $E2$-transition strengths. However, state mixing between three negative-parity bands is rather strong, as shown later; hence, the negative-parity band structure cannot be strictly defined. For the experimental states of the negative-parity bands, we adopt the tentative band assignment used in Ref. [2].

The calculated and experimental energy spectra are plotted in Fig. 1. It should be commented that the experimental 4^- and 5^- states are uncertain except for the 4^-(9.30 MeV) and 5^-(11.59 MeV) states. The present calculation well reproduces the level spacing in each band and qualitatively describes the energy ordering of the positive- and negative-parity bands, but it generally overestimates the bandhead energies of the excited bands. Higher-order effects beyond the present structure model may be a reason for such overestimation. In the next paper [63], we will present an improved result of the AMD calculation for the $K^\pi = 2^+$ band.

The calculated root-mean-square radii (R) of the ground and excited states and the electric-quadrupole moment (Q) of the 2^+_1 state are listed in Table I. The calculated values $R = 3.02$ fm (of the ground state) and $Q = -15.1$ $e$fm^2 (of the 2^+_1 state) are consistent with the observed values of $R = 2.941(2)$ fm and $Q = -16.6(6)$ $e$fm^2. The calculation predicts slightly larger radii for the $K^\pi = 0^-$ and $K^\pi = 1^-$

TABLE II. $E2$-transition strengths of ^{24}Mg. The experimental values $B_{\exp}(E2)$ for positive- and negative-parity states are from Refs. [3,62] and Ref. [2], respectively. The theoretical values $B_{\rm th}(E2)$ obtained by the VAP calculation are listed together with the renormalization factors $f^{\rm tr}$ used for the reaction calculations. The $E2$-transition strengths are in units of e^2fm^4.

J_i (band)	J_f (band)	exp $B_{\exp}(E2)$	AMD $B_{\rm th}(E2)$	$f^{\rm tr}$
2^+_1 ($K = 0$)	0^+_1 ($K = 0$)	88.4(4.1)	55.4	1.26
4^+_1 ($K = 0$)	2^+_1 ($K = 0$)	160(16)	72.8	1.48
3^+_1 ($K = 2$)	2^+_2 ($K = 2$)	240(30)	103.1	
4^+_2 ($K = 2$)	2^+_2 ($K = 2$)	77(10)	36.2	1.46
4^+_2 ($K = 2$)	3^+_1 ($K = 2$)		73.3	
2^+_2 ($K = 2$)	0^+_1 ($K = 0$)	8.0(0.8)	2.1	1.95
2^+_2 ($K = 2$)	2^+_1 ($K = 0$)	12.2(0.9)	0.6	1$^{\rm a}$
3^+_1 ($K = 2$)	2^+_1 ($K = 0$)	10.3(1.2)	3.1	
4^+_2 ($K = 2$)	2^+_1 ($K = 0$)	4.1(0.4)	2.9	1.19
4^- ($K = 3$)	3^-_1 ($K = 3$)	119(25)	76.9	
5^- ($K = 3$)	3^-_1 ($K = 3$)	19(6)	14.9	
5^- ($K = 3$)	4^- ($K = 3$)	152(45)	48.7	
3^-_2 ($K = 0$)	1^-_1 ($K = 0$)		67.9	
5^- ($K = 0$)	3^-_2 ($K = 0$)	82(27)	81.4	
2^-_1 ($K = 1$)	1^-_2 ($K = 1$)		132	
3^- ($K = 1$)	1^-_2 ($K = 1$)		45.8	
3^- ($K = 1$)	2^-_1 ($K = 1$)		32.9	
4^- ($K = 1$)	2^-_1 ($K = 1$)		101.5	
4^- ($K = 1$)	3^- ($K = 1$)		27.6	
5^- ($K = 1$)	4^- ($K = 1$)		5.6	
5^- ($K = 1$)	3^- ($K = 1$)	90(16)	91.5	
3^-_2 ($K = 0$)	1^-_2 ($K = 1$)		17.7	
3^-_2 ($K = 0$)	2^-_1 ($K = 1$)		34.1	
5^- ($K = 0$)	4^- ($K = 1$)		19.9	
3^- ($K = 1$)	1^-_1 ($K = 0$)		36.4	
4^- ($K = 1$)	3^-_2 ($K = 0$)		30.3	
5^- ($K = 1$)	3^-_2 ($K = 0$)	2.7(0.7)	20.1	
5^- ($K = 0$)	4^- ($K = 3$)		10.3	
5^- ($K = 3$)	3^-_2 ($K = 0$)		14.4	

$^{\rm a}$no renormalization.

bands, because they have deformations, than those of the $K^\pi = 0^+$ and $K^\pi = 3^-$ bands, but the difference is small.

In Table II, the calculated $E2$-transition strengths are compared with the experimental data. For the negative-parity states, the assignment of the $K^\pi = 3^-$, $K^\pi = 0^-$, and $K^\pi = 1^-$ bands is done tentatively for calculated states having remarkably strong $E2$ transitions. However, strong $E2$ transitions are also obtained for interband transitions, in particular, between the $K^\pi = 0^-$ and $K^\pi = 1^-$ bands, and indicate strong band mixing, The present AMD calculation qualitatively describes the experimental $E2$-transition strengths, but the quantitative agreement with the data is unsatisfactory. The theoretical strengths $B_{\rm th}(E2)$ tend to underestimate the experimental data $B_{\exp}(E2)$, possibly because the present AMD

TABLE III. $E\lambda(C\lambda)$ and isoscalar ISλ transition strengths to the 0_1^+ state for the J^π ($J = \lambda$) states of ²⁴Mg. For the experimental values, $B(E\lambda; \lambda^\pi \to 0_1^+)$ from the γ-decay data [62,65], $B(C\lambda; \lambda^\pi \to 0_1^+)$ from the (e, e') data [7,9,10], $B(\text{IS}\lambda; \lambda^\pi \to 0_1^+)/4$ from the (α, α') data [28], and $B(C\lambda; \lambda^\pi \to 0_1^+)$ from the (π, π') data [11] are listed. For theoretical values, the original values $B_{\text{th}}(\text{IS}\lambda)/4$ before renormalization and the renormalized values $(f^{\text{tr}})^2 B_{\text{th}}(\text{IS}\lambda)/4$ used for the reaction calculations are shown together with the adopted renormalization factors f^{tr}. Transition strengths are in units of $e^2\text{fm}^{2\lambda}$ for the $\lambda = 2$, $\lambda = 3$, and $\lambda = 4$ transitions, and $e^2\text{fm}^6$ for the isoscalar dipole (IS1) transitions.

| | γ decays | (e, e') | (e, e') | (α, α') | (π, π') | AMD | | |
| | $B(E\lambda)$ | $B(C\lambda)$ | $B(C\lambda)$ | $B(\text{IS}\lambda)/4$ | $B(C\lambda)$ | $B(\text{IS}\lambda)/4$ | | |
J^π (band)	[62,65]	[9,10]	[7]	[28]	[11]	original	normalized	f^{tr}
2_1^+ $(K=0)$	88.4(4.1)	90.6(7.0)	105(5)	84	108	54	86	1.26[a]
2_2^+ $(K=0)$	8.0(0.8)	5.48(0.60)	5.26(1.2)	14	6.7	2.0	7.7	1.95[a]
4_1^+ $(K=0)$		200(30)		1200		1.1	1.1	1.0[b]
4_2^+ $(K=0)$		4800(600)	4700(1100)	4700	2900	1740	4800	1.66[c]
3_1^- $(K=3)$	221(44)	80	190(30)	190	136	28	80	1.68[c]
3_2^- $(K=0)$		226	290(30)	280	226	89	226	1.59[c]
3^- $(K=1)$						0.1	0.1	1.0[b]
1_1^- $(K=0)$						3.1	19.3	2.5[d]
1_2^- $(K=1)$						4.3	17.2	2.0[d]

[a] f^{tr} determined to fit $B(E\lambda)$ from γ decays.
[b] No renormalization.
[c] f^{tr} determined to fit $B(C\lambda)$ from (e, e') data [9,10].
[d] f^{tr} determined to fit the charge-form factors from (e, e') data [9,10].

calculation is a simple version based on the single-Slater description of spherical Gaussians and may be insufficient to describe the large collectivity of deformations in ²⁴Mg. To use the transition densities in the MCC calculations, we introduce the renormalization factors $f^{\text{tr}} = (B_{\text{exp}}/B_{\text{th}})^{1/2}$ to fit the observed values $B_{\text{exp}}(E2)$, as mentioned previously. The f^{tr} values adopted in the present MCC calculation are given in Table II. The factors $f^{\text{tr}} = 1.19$–1.95 are needed to fit the $B_{\text{exp}}(E2)$ values. It should be noted that bare charges of nucleons are adopted in the AMD framework, unlike the shell models in which the effective charges of protons and neutrons are usually required. If we introduce the effective charges, the values of $f^{\text{tr}} = 1.19$–1.95 obtained in the present AMD result correspond to the enhancement $\delta = 0.1$–0.5 for the effective charges $e_p^{\text{eff}} = 1 + \delta$ and $e_n^{\text{eff}} = \delta$ of the protons and neutrons, which are comparable to or even smaller than standard shell-model values $\delta = 0.3$–0.5 for sd-shell nuclei [66–69].

In Table III, the results for the inelastic transition strengths from the ground state are listed in comparison with the experimental values measured by γ decays and evaluated by electron, α, and pion scattering. For the $E2$, $E3$, and $E4$ transitions, the calculated values $B(\text{IS}\lambda)/4$ of the isoscalar component are compared with the experimental data for $B(E\lambda)$, $B(C\lambda)$, and $B(\text{IS}\lambda)/4$. For the dipole transitions, the calculated values of the isoscalar dipole (IS1) transition strengths are shown in the table. For use in the MCC calculations, the renormalization factors f^{tr} for the $0_1^+ \to 3_1^-$, $0_1^+ \to 3_2^-$, and $0_1^+ \to 4_2^-$ transitions are determined to fit the $B(C\lambda)$ values that were evaluated from the (e, e') data. For the IS1 transitions, f^{tr} are determined to fit the charge-form factors measured by the (e, e') experiments. As a result of this fitting, the renormalization factors for the $4_2^+ (K^\pi = 2^+)$,

$3_1^- (K^\pi = 3^-)$, $3_2^- (K^\pi = 0^-)$, $1_1^- (K^\pi = 0^-)$, and $1_2^- (K^\pi = 1^-)$ states are obtained in the range of $f^{\text{tr}} = 1.59$–2.5, which again means that the collectivity of these excited states is somewhat underestimated by the present AMD calculation.

For the $4_1^+ (K^\pi = 0^+)$ state, a remarkably weak $\lambda = 4$ transition was observed in the (e, e') experiment [9]. The $0_1^+ \to 4_1^+$ transition strength is more than one order smaller than that for the $0_1^+ \to 4_2^+$ transition meaning that the $\lambda = 4$ strength from the ground state is dominantly concentrated not in the $4_1^+ (K^\pi = 0^+)$ state but rather in the $4_2^+ (K^\pi = 2^+)$ state. The calculation describes this trend of weak $\lambda = 4$ transition in the $K^\pi = 0^+$ ground band, but quantitatively it is too weak compared with the observed data and hence $f^{\text{tr}} = 1$ (no renormalization) is adopted for this transition in the MCC calculation. The leading feature of the $4_1^+ (K^\pi = 0^+)$ state is the strong in-band $E2$ transition to the $2_1^+ (K^\pi = 0^+)$ state, whereas the $E4$ transition is a higher-order effect. We can say that the present calculation qualitatively reproduces the leading feature of the 4_1^+ state but fails to describe the higher-order effect.

B. Intrinsic structure of ²⁴Mg: AMD results

To discuss the intrinsic structure of the ground and excited bands, we analyze the single-Slater AMD wave functions for the dominant configurations of the bandhead states, which are obtained by VAP. Such a simple analysis is useful for obtaining an intuitive understanding of the leading features though the final wave functions are affected by state mixing and in-band structure change.

Figure 2 shows the density distribution of the intrinsic wave functions before the parity and total-angular-momentum projections for the $0_1^+ (K^\pi = 0^+)$, $3_1^+ (K^\pi = 2^+)$, $3_1^- (K^\pi = $
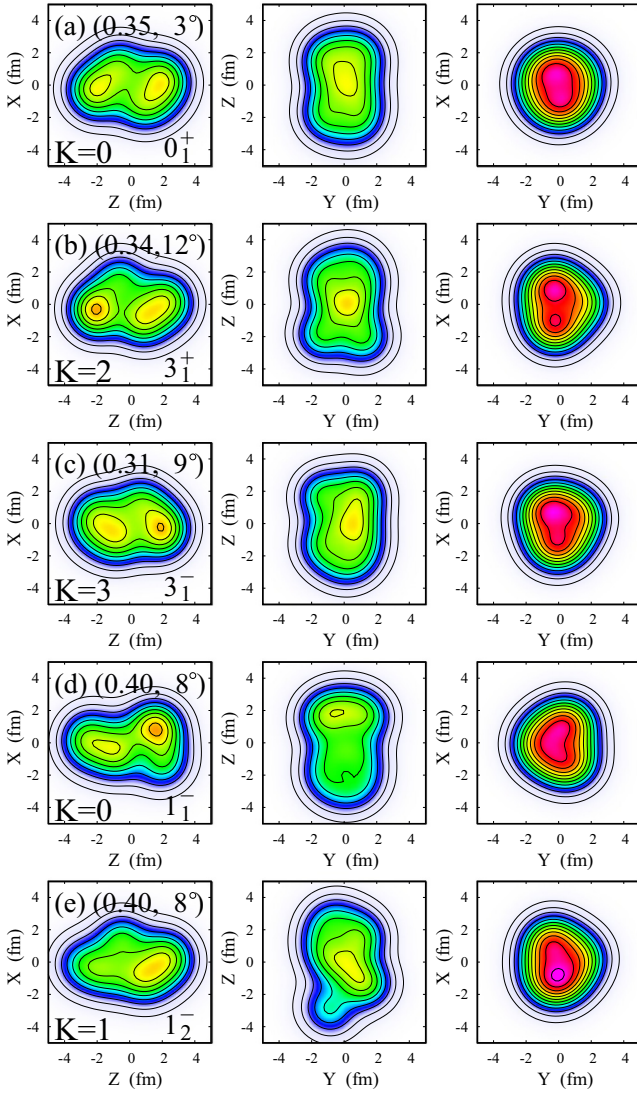
FIG. 2. Density distribution of intrinsic wave functions prior to the parity and total-angular-momentum projections for the $0_1^+(K^\pi = 0^+)$, $3_1^+(K^\pi = 2^+)$, $3_1^-(K^\pi = 3^-)$, $1_1^-(K^\pi = 0^-)$, and $1_1^-(K^\pi = 1^-)$ states, as obtained by AMD. The integrated density projected onto the X-Z, Y-Z, and Y-X planes is plotted in the left, middle, and right panels, respectively, by contours with the interval of 0.1 fm^{-2} interval. For each state, the axes are chosen to be the principal axes of intrinsic deformation as $\langle ZZ \rangle \geqslant \langle YY \rangle \geqslant \langle XX \rangle$ and $\langle XY \rangle = \langle YZ \rangle = \langle ZX \rangle = 0$. The deformation parameters (β, γ) calculated from the expectation values, $\langle ZZ \rangle$, $\langle YY \rangle$, and $\langle XX \rangle$, are shown in the left panels.

3^-), $1_1^-(K^\pi = 0^-)$, and $1_1^-(K^\pi = 1^-)$ states. The quadrupole-deformation parameters β, γ, which are calculated from the expectation values of $\langle ZZ \rangle$, $\langle YY \rangle$, and $\langle XX \rangle$ for the intrinsic wave functions, are also shown. The $K^\pi = 0^+$ band has an approximately prolate deformation with a ^{12}C + ^{12}C clustering feature. The deformation is $\beta = 0.35$ in the 0_1^+ state, and gradually decreases to $\beta = 0.33$ and 0.29 in the $2_1^+(K^\pi = 0^+)$ and $4_1^+(K^\pi = 0^+)$ states, respectively.

The excited bands have triaxial deformations with ^{12}C + 3α-like cluster structures. In particular, the $K^\pi = 2^+$

band has the largest triaxiality as $\gamma = 12°$, because of the 2α clustering around the ^{12}C + α core part as shown in Fig. 2(b). The β deformation of the $K^\pi = 2^+$ band is approximately the same as that of the ground state, meaning that this band can be understood as the $K^\pi = 2^+$ sideband of the $K^\pi = 0^+$ ground band. For the negative-parity bands, the $K^\pi = 3^-$ band has almost the same β deformation as the ground state, whereas the $K^\pi = 0^-$ and $K^\pi = 1^-$ bands have larger deformations as $\beta = 0.40$. In the intrinsic densities for the $K^\pi = 0^-$ and $K^\pi = 1^-$ bands shown in Figs. 2(d) and 2(e), one can see that the reflection symmetry for $Z \leftrightarrow -Z$ in the Z direction is broken in the $K^\pi = 0^-$ band owing to the asymmetric structure of ^{12}C + ^{12}C clustering, whereas the reflection symmetry for $Y \leftrightarrow -Y$ in the Y direction is broken in the $K^\pi = 1^-$ band. These symmetry-broken shapes produce two types of negative-parity excitations with quanta of $K = 0$ and $K = 1$. This result for the $K^\pi = 0^-$ and $K^\pi = 1^-$ bands is similar to that for the deformed AMD result for low-lying 1^- states, as found in Ref. [33], although that calculation yielded the reverse ordering of the $K^\pi = 0^-$ and $K^\pi = 1^-$ energies.

The negative-parity bands are built on different kinds of excitation modes; these excitations contain large-amplitude dynamics and cluster correlations beyond the single-particle excitations on the ground state in the mean-field picture. However, with the help of single-particle analyses of the present AMD configurations, we can associate the leading aspects of the $K^\pi = 3^-$ and $K^\pi = 1^-$ bands of ^{24}Mg with $1p$-$1h$ excitations in the deformed state. In Fig. 3, we show the density difference between the positive- and negative-parity components in each bandhead state of the $3_1^-(K^\pi = 3^-)$, $1_1^-(K^\pi = 0^-)$, and $1_1^-(K^\pi = 1^-)$ states. For each intrinsic wave function, the positive- and negative-parity components are normalized as $|P^\pi \Phi_{\mathrm{AMD}}\rangle / \sqrt{\langle P^\pi \Phi_{\mathrm{AMD}} | P^\pi \Phi_{\mathrm{AMD}} \rangle}$, and the positive-parity density is subtracted from the negative-parity density. This density difference may reflect the $1p$-$1h$ feature, by which positive- and negative-sign contributions correspond to particle and hole densities, respectively. In the density difference for the $K^\pi = 3^-$ band [Fig. 3(a)], the hole contribution is remarkable in the inner region and indicates significant contributions by single-particle excitations from the p shell to the sd shell; this is associated with the $K^\pi = 3^-$ excitation of the ^{16}O core due to ^{12}C + α clustering. The $1_2^-(K^\pi = 1^-)$ state clearly shows the $(sd)^{-1}(fp)$ feature shown in Fig. 3(c), which is predominantly interpreted as the $(0, 1, 1)^{-1}(0, 0, 3)$ configuration in terms of the single-particle description (n_x, n_y, n_z) of the three-dimensional oscillator quanta. This configuration of the $K^\pi = 1^-$ band corresponds to the toroidal dipole excitation of the deformed state, which was obtained in Refs. [30,31,33] not as the second 1^- state but as the lowest 1^- state. For the $1_1^-(K^\pi = 0^-)$ state, the single-particle aspects are unclear, but one can see a signal from the mixture of the $(0, 1, 1)^{-1}(0, 1, 2)$ and $(0, 0, 2)^{-1}(0, 0, 3)$ configurations, as caused by the $K^\pi = 0^-$ excitation of the cluster mode [see the left panel of Fig. 3(b)].

C. Diagonal and transition densities and charge-form factors

In Fig. 4, we show the matter densities of the ground and excited states. The $K^\pi = 0^-$ and $K^\pi = 1^-$ bands have slightly
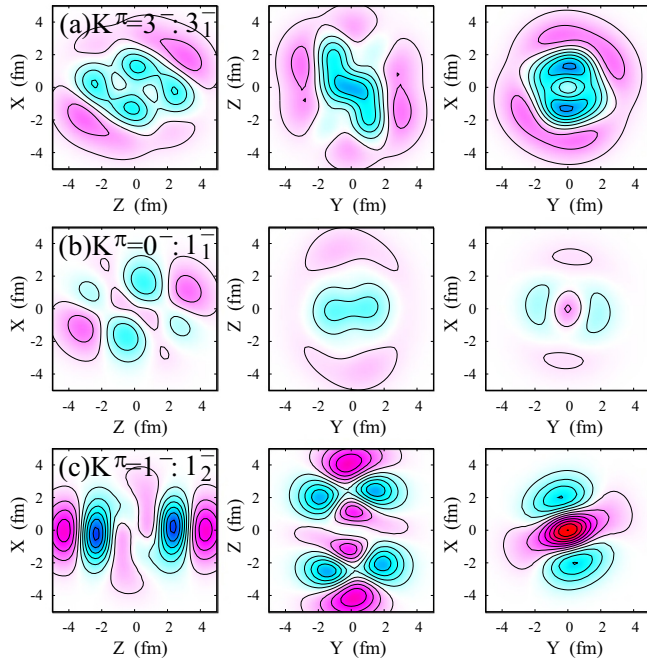
FIG. 3. Density difference between the positive-parity and negative-parity components in the intrinsic states of the bandhead states; (a) 3_1^- ($K^\pi = 3^-$), (b) 1_1^- ($K^\pi = 0^-$), and (c) 1_2^- ($K^\pi = 1^-$). For each state, The intrinsic density of the positive-parity component is subtracted from that of the negative-parity component, and the difference of the integrated densities is projected onto the Z-X, Y-Z, and Y-X planes, as shown in the left, middle, and right of the figure, respectively. The intrinsic axes are chosen to for consistency with Fig. 2. The contour interval is 0.003 fm^{-2}, and the red (blue) color map indicate positive (negative) values.

broader density tails than do the $K^\pi = 0^+$ and $K^\pi = 3^-$ bands due to larger deformations; however, the difference in the diagonal density is small.

Let us discuss the properties of the form factors and transition densities. For the calculated results, we show the renormalized form factors and transition densities, which are multiplied by the factors f^{tr} given in Table III. The renormalized inelastic charge-form factors for the positive- and negative-parity states are compared with the experimental data measured by (e, e') in Figs. 5 and 6, respectively. The calculated and experimental elastic charge-form factors are also shown in Fig. 5.

The calculated form factors reproduce the state-dependent shapes of the observed form factors (except for the 4_1^+ state) and after the renormalization, they agree well with the experimental data. In particular, the calculation successfully reproduces the two-peak structure of the 1_1^- and 3_2^- form factors for transitions to the $K^\pi = 0^-$ band. Hence, the strong-state dependence of the charge-form factors observed in the 1_1^-, 1_2^-, 3_1^-, and 3_2^- states is well described. From these good agreements with the data, the present assignment for the calculated states to the observed states can be said to be reasonable. The form factors predicted for the 3_3^- state are remarkably small and their shape is inconsistent with neither the 3_1^- nor 3_2^- states meaning that this state has a quite differ-
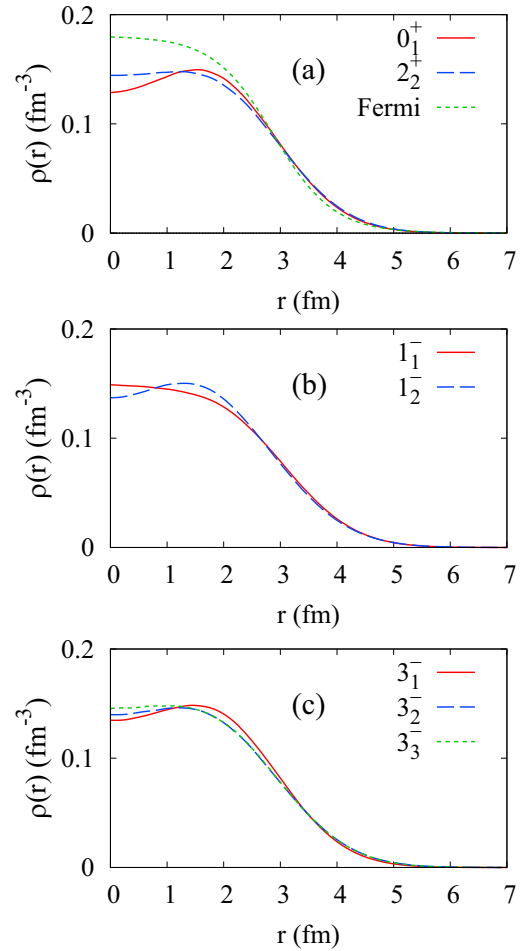

FIG. 4. The matter densities of ^{24}Mg. The Fermi density $\rho_{\mathrm{Fermi}}(r) = \rho_0[1 + \exp(\frac{r-c}{t/4.4})]^{-1}$ with $c = 2.876$ fm and $t = 2.333$ fm is also shown in (a).

ent character from the lowest two 3^- states. The form factors observed for the 4_1^+ state are much smaller than those for the 4_2^+ state [9]. The present AMD calculation yields small form factors for the 4_1^+ state, which are comparable to the experimental data; however, the shape of the form factors is inconsistent with that is observed.

The renormalized transition densities are shown in Fig. 7. The 1_1^- and 3_2^- states in the $K^\pi = 0^-$ band show characteristics quite different from those of normal IS1 and $E3$ transitions. As discussed previously, the calculated form factors for these states have narrow two-peak structures, which correspond to the transition density broadly distributed in the outer region with an extra node in the inner region [see Figs. 7(c) and 7(d)]. This unusual behavior is caused by the $K^\pi = 0^-$ excitation of the asymmetric cluster structure, which involves radial excitations of higher-nodal orbits, including the $(1s)^{-1}(1p)$ configuration in the higher shells. Such nodal behavior cannot be described by collective models and indicates the importance of a microscopic description of the inelastic transitions in the $K^\pi = 0^-$ band. To clarify this, we also show the collective-model-transition density with the Fermi-type Tassie form given by the derivative form
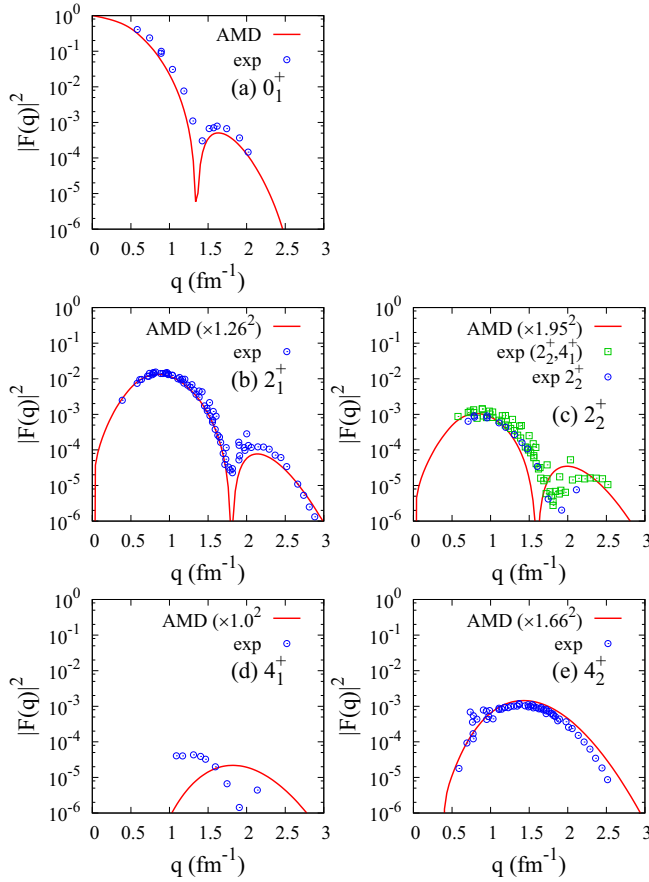
FIG. 5. Square of the charge-form factors of the elastic and inelastic processes for the positive-parity states of ^{24}Mg. For the calculated result, the square of the renormalized form factors $F(q)$ multiplied by the $f^{\rm tr}$ values in Table III are plotted. The experimental data were measured by electron scattering [4,6–9]. In Refs. [4,6,8] for the 2^+_2(4.24 MeV) state, the 4^-_1(4.12 MeV) contributions were not separated.

$$\rho^{\rm tr}_{\rm Tassie}(r) \propto r^{\lambda-1}\partial\rho_{\rm Fermi}(r)/\partial r \text{ of the Fermi density}$$

$$\rho_{\rm Fermi}(r) = \frac{\rho_0}{1 + \exp\left(\frac{r-c}{t/4.4}\right)}, \tag{5}$$

where the parameters c and t are set to be $c = 2.876$ fm and $t = 2.333$ fm, respectively, which have been adjusted in Ref. [7] to fit the elastic form factors measured by electron scattering. Note that the value of $2.876 = \sqrt{2.985^2 - 0.8^2}$ fm for the point-nucleon transition density is derived from the original value of $c = 2.985$ fm from Ref. [7] for the charge-form factor considering the proton charge-form factor. In Fig. 7, we compare the collective-model-transition density for the 2^+, 4^+, and 3^- states, which is normalized to fit the $E\lambda$-transition strengths from the 0^+_1 state to the 2^+_1, 4^+_2, and 3^-_1 states so that $B(E\lambda) = |\int r^{l+2}\rho^{\rm tr}_{\rm Tassie}(r)dr|^2/(2J_i + 1)$ ($J_i = 0$ is the total angular momentum of the initial state.)

This collective-model-transition density yields a single-peak structure at the nuclear surface, which seems reasonable for the $0^+ \to 2^+_1$, $0^+ \to 4^+_2$, and $0^+ \to 3^-_1$ transitions but fails
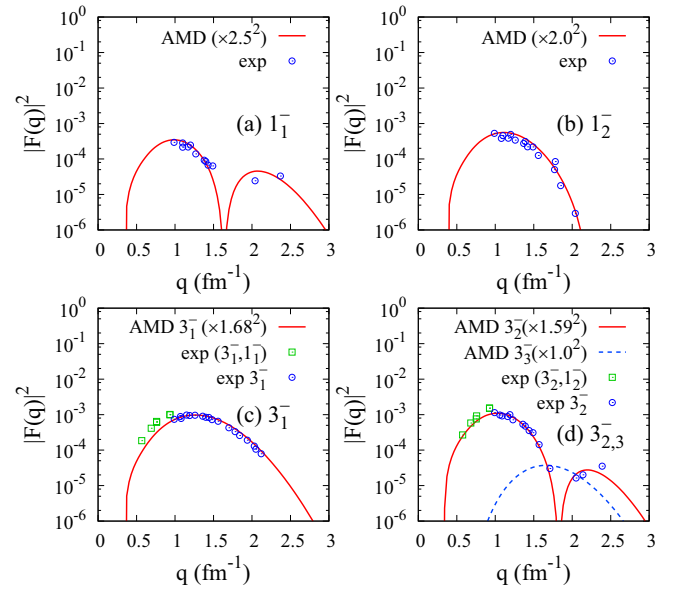

FIG. 6. Same as Fig. 5 but for the negative-parity states. The experimental data are taken from Refs. [7,10]. In the data from Ref. [7] for the 3^-_1 (7.62 MeV) and 3^-_2 (8.36 MeV) states, the 1^-_1 (7.56 MeV) and 1^-_2 (8.44 MeV) contributions were not separated.

to describe the peak position of the $0^+ \to 3^-_2$ transition in the outer region.

IV. PROTON AND α SCATTERING: MCC+AMD RESULTS

The MCC+AMD calculations are performed for proton and α scattering using the calculated diagonal and renormalized transition densities. Our major interest is in extracting structural information, particularly to confirm the band assignment of the negative-parity states via reaction analysis of the inelastic cross sections. We intend to determine how the state dependence of the transition densities affects the cross sections, and whether inelastic scattering can probe the properties of three kinds of negative-parity excitations.

We calculate the elastic and inelastic cross sections of proton scattering at incident energies of $E_p = 40$ MeV, 49 MeV, 65 MeV, and 100 MeV, as well as α scattering at $E_\alpha = 104$ MeV, 120 MeV, 130 MeV, and 386 MeV, and compare the results with the existing data. To see the CC effects, the one-step calculation of the distorted wave Born approximation (DWBA) is also performed using the same inputs.

A. Proton scattering off ^{24}Mg

The calculated cross sections of proton scattering are shown in Fig. 8 and compared with the experimental data. The MCC+AMD calculation reasonably reproduces amplitudes of the proton elastic and inelastic cross sections in this energy region except for the 4^+_1 cross sections. It also qualitatively describes the diffraction patterns of the cross sections, though it is not precise enough to reproduce the dip structures of low-energy-backward and high-energy scattering, mainly because
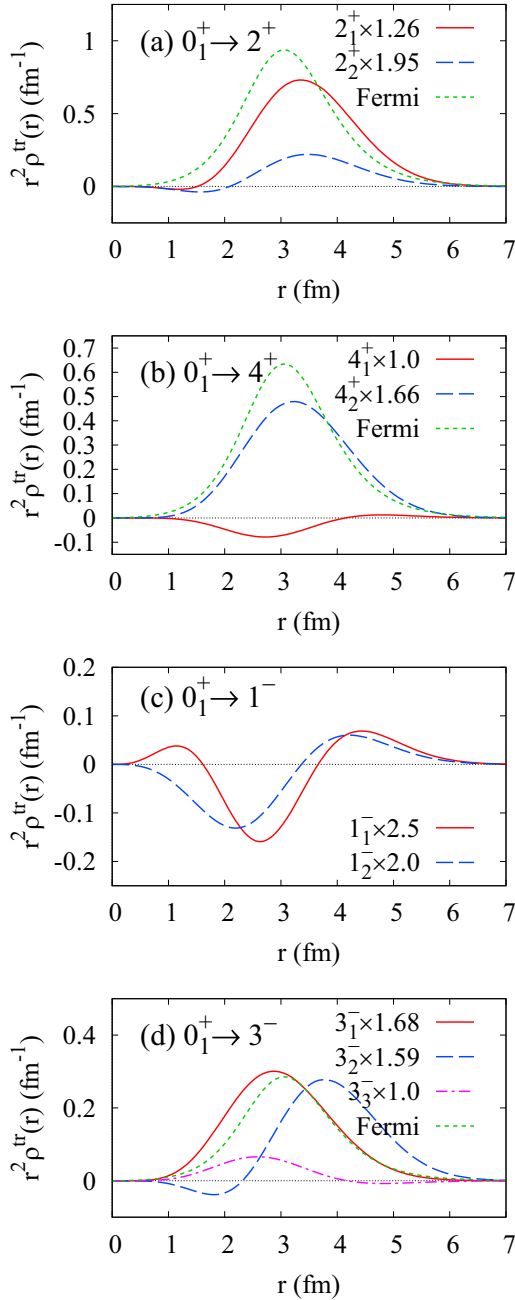
FIG. 7. The isoscalar components (average of the proton and neutron components) of the transition densities of ^{24}Mg. The renormalized transition densities multiplied by the f^{tr} values in Table III are plotted. For transitions to the 2^+, 4^+, and 3^- states, the collective-model-transition density of the Fermi-type Tassie form $\rho^{\mathrm{tr}}_{\mathrm{Tassie}}(r) \propto r^{\lambda-1}\partial\rho_{\mathrm{Fermi}}(r)/\partial r$ is also shown for comparison. $\rho^{\mathrm{tr}}_{\mathrm{Tassie}}(r)$ is normalized to fit the $E\lambda$-transition strengths from the 0^+_1 state to the 2^+_1, 4^+_2, and 3^-_1 states.

the spin-orbit potentials are ignored in the reaction calculation. Quantitatively, the calculation somewhat underestimates the amplitudes of the 3^-_1 and 4^+_2 cross sections.

Let us discuss the state dependence of the proton-scattering cross sections for the $3^-_1(K^\pi = 3^-)$ and $3^-_2(K^\pi = 0^-)$ states.

Both 3^- states have strong $\lambda = 3$ transitions from the ground state, and are therefore strongly populated through inelastic scattering. However, as observed in the (e, e') experiment, the two 3^- states represent the shape difference of the form factors because they have different origins of the excitation modes. Comparing the calculated cross sections of the 3^-_1 and 3^-_2 states, one can see a difference in the ratio of the first- and second-peak amplitudes; the second peak of the 3^-_2 cross sections is suppressed at $E_p = 100$ MeV. This suppression at the second peak for the 3^-_2 state can be understood by the exotic character of the $0^+_1 \rightarrow 3^-_2$ transition density having a nodal structure with the enhanced outer amplitudes shown in Fig. 7(d). In the (p, p') data at $E_p = 100$ MeV, the 3^-_2 cross sections fall rapidly compared with the 3^-_1 state and support the second-peak suppression of the calculated cross sections for the $3^-_2(K^\pi = 0^-)$ state. A similar trend is also seen in the (p, p') data at $E_p = 65$ MeV, but the difference between the 3^-_1 and 3^-_2 cross sections is not clearly seen at $E_p = 40$ MeV, for which the correspondence between transition densities and cross sections is not as direct as high energies because of distortion effects.

In the comparison of the CC results with the one-step (DWBA) cross sections of proton scattering, the CC effects for the first and second peaks are found to be minor, except at the 1^-_1 and 4^+_1 cross sections. The $1^-_1(K^\pi = 0^-)$ cross sections are strongly affected by the CC effect mainly because of the strong in-band $\lambda = 2$ transition of the 1^-_1-3^-_2 coupling in the $K^\pi = 0^-$ band. This CC effect suppresses the forward cross sections in the $\theta \leqslant 20°$ region. Hence, the calculation describes the enhanced cross sections in the $\theta = 20–40°$ region observed in $E_p = 40$ MeV and 65 MeV proton scattering. On the other hand, for the $1^-_2(K^\pi = 1^-)$ cross sections, such CC effects are not significant, even though the in-band $\lambda = 2$ transition in the $K^\pi = 1^-$ band is as large as that in the $K^\pi = 0^-$ band. The weak CC effect for the $1^-_2(K^\pi = 1^-)$ state results from the fact that the inelastic transition $0^+_1 \rightarrow 3^-_3(K^\pi = 1^-)$ is weak compared with the $0^+_1 \rightarrow 3^-_2(K^\pi = 0^-)$ transition. It should be noted that the CC effect changes the angular distribution of the 1^-_1 and 4^+_1 cross sections, which indicates that this CC effect is not just a matter of a constraint on the unitarity.

Thus, we can argue that the present assignments of the $3^-_1(7.62$ MeV$)$ to the $K^\pi = 3^-$ band and the $1^-_1(7.56$ MeV$)$ and $3^-_2(8.36$ MeV$)$ states to the $K^\pi = 0^-$ band are supported by the observed proton-scattering cross sections.

B. α scattering off ^{24}Mg

The results for α scattering are shown in Fig. 9. The MCC+AMD calculation successfully reproduces the observed elastic and inelastic cross sections of α scattering in the energy range of $E_\alpha = 100–400$ MeV except in the 4^+_1 state. In the comparison with the one-step cross sections, the CC effects in the α-scattering cross sections are generally significant, except for the forward cross sections of the 0^+_1, 2^+_1, 2^+_2, and 1^-_2 states. The 4^+_1 cross sections are hindered by the CC effect of the $\lambda = 2$ coupling with the 2^+_1 and 2^+_2 states. Moreover, the 1^-_1 cross sections are mainly suppressed because of the $\lambda = 2$ coupling with the 3^-_2 state. For the 3^-_2
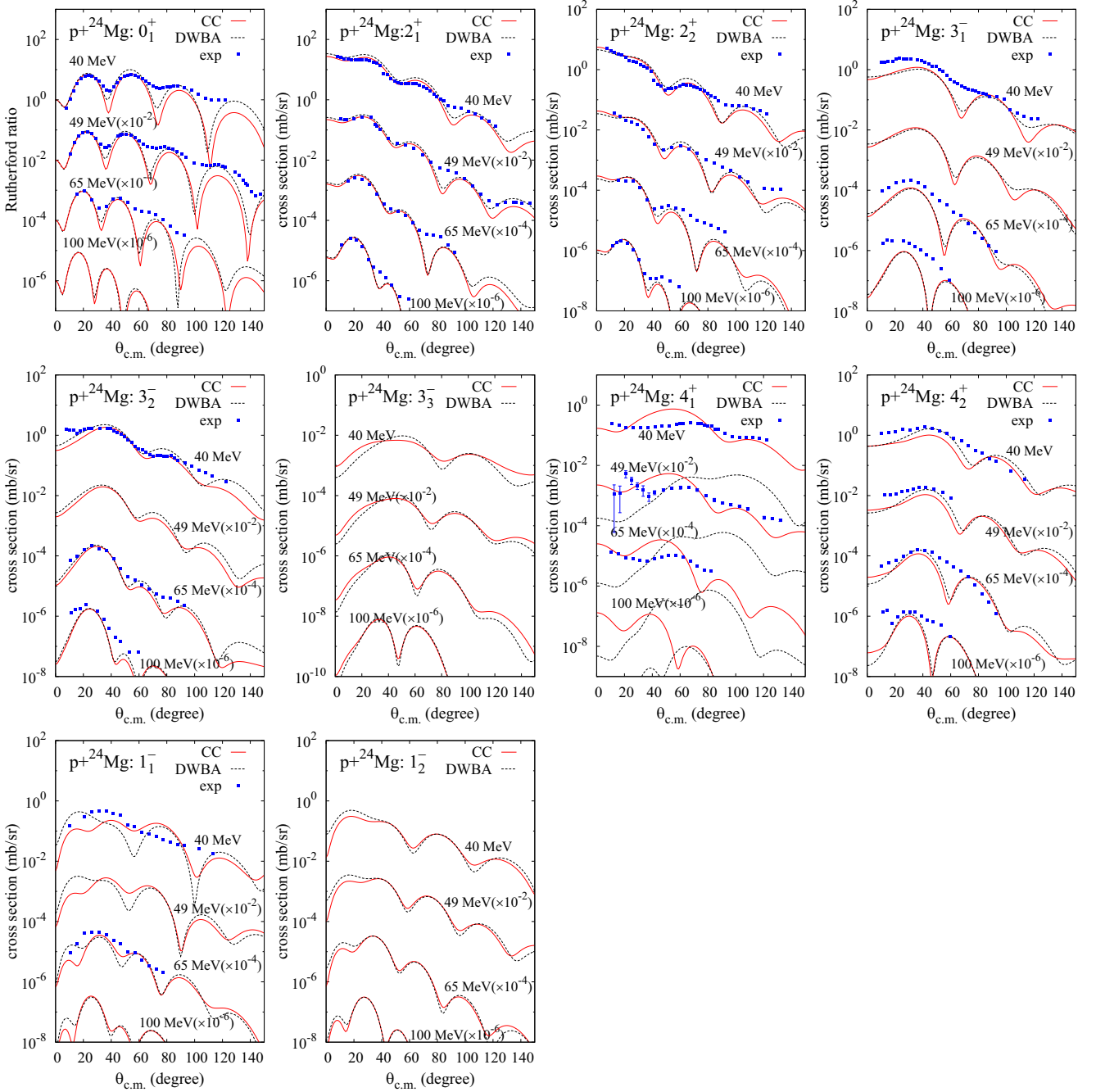
FIG. 8. Cross sections of proton scattering off ^{24}Mg at incident energies of $E_p = 40$, 49, 65, and 100 MeV, as calculated with MCC+AMD (solid lines with label "CC") and DWBA (dotted lines with label "DWBA"). For the 4_1^+ state, the DWBA cross sections are two orders smaller than the CC cross sections. Experimental data are cross sections at $E_p = 40$ MeV [15,16], 49 MeV [13], 65 MeV [17,70], and 100 MeV [18,70].

state, the CC effect somewhat suppresses the cross sections but the effect is not as large as in the 1_1^- and 4_2^+ cases. When the CC effect does not change the angular distribution of the cross section and decreases its magnitude, it can be understood as a result of the constraint on the unitarity. As is well known, in the one-step calculation, the unitarity of the S matrix is not respected at all and, in general, the total flux of the outgoing waves exceeds the physical result. This issue

can be resolved by including the higher-order transitions. One can interpret the CC effect on the cross sections to the 4_2^+, 1_1^-, and 3_2^- states in this way. A striking finding is the CC effect on the 3_1^- cross section; it enhances the 3_1^- cross sections mainly due to the $\lambda = 3$ coupling with the 2_1^+ state and the $\lambda = 2$ self-coupling. As the incident energy increases, the CC effects become small but are still non-negligible, even at $E_\alpha = 386$ MeV. The state and energy dependencies of the CC
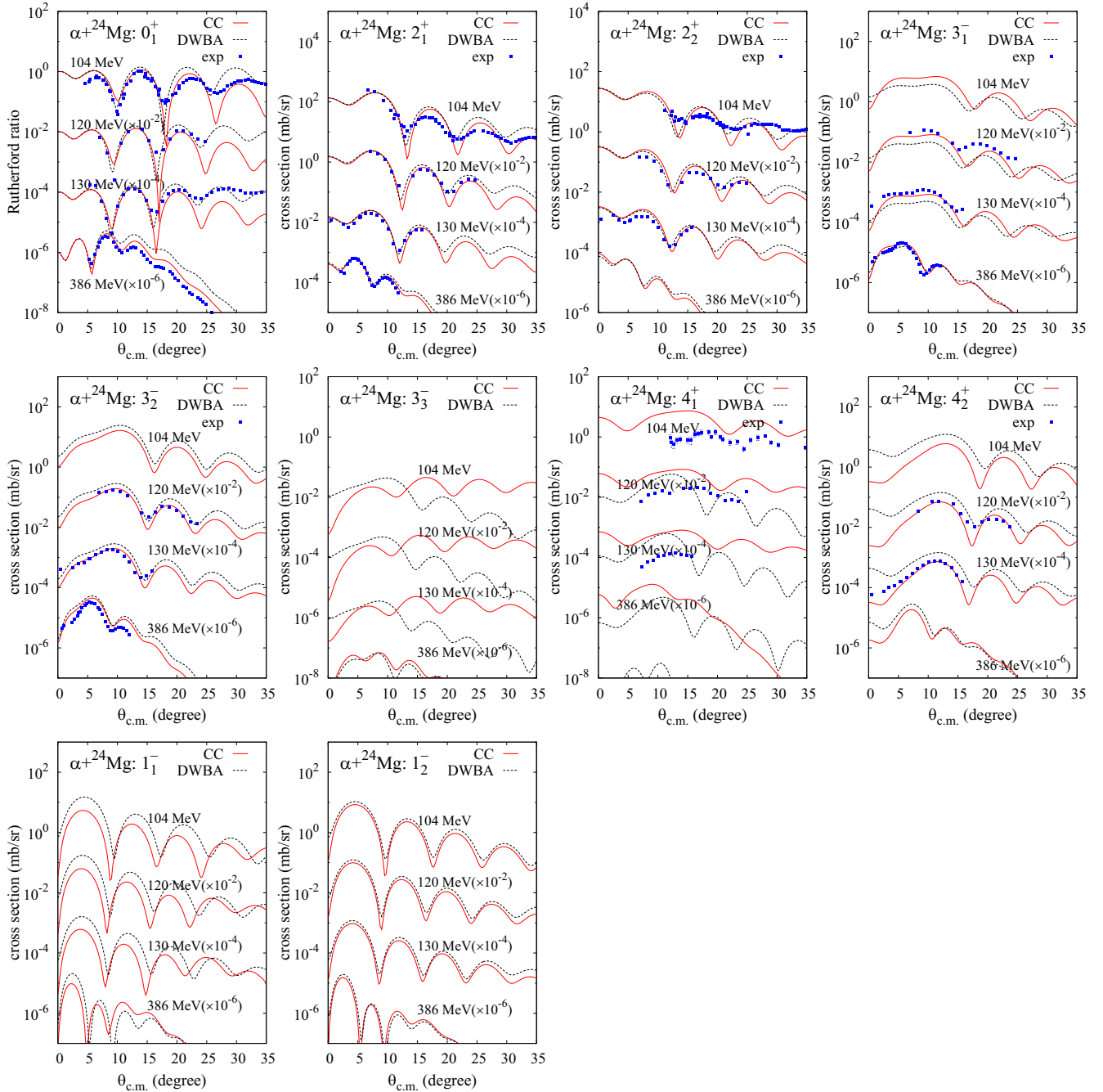
FIG. 9. Cross sections of α scattering off ^{24}Mg at incident energies of $E_\alpha = 104$, 120 MeV, 130 MeV, and 386 MeV, as calculated with MCC+AMD (solid lines labeled "CC") and DWBA (dotted lines labeled "DWBA"). For the 4_1^+ state, the DWBA cross sections are two-order smaller than the CC cross sections. The experimental data are cross sections at $E_\alpha = 104$ MeV [27,70], 120 MeV[28], 130 MeV [29], and 386 MeV [29].

effects found in the calculation are essential for reproducing the amplitude of the observed α-scattering cross sections of the 4_2^+, 3_1^-, and 3_2^- states.

Let us discuss the state dependence of the cross sections of the two 3^- states. In the calculated cross sections for these states, a difference is observed in the first-peak shape. The 3_1^- cross sections show a broad peak, whereas the 3_2^- cross sections present a narrow peak slightly shifted to backward angles. This difference is observed

in the experimental data over a wide energy range from $E_\alpha = 120$–386 MeV. This result for the α scattering supports again the assignment of the bandhead states of the $K^\pi = 3^-$ and $K^\pi = 0^-$ bands to the $3_1^-(7.62$ MeV) and $3_2^-(8.36$ MeV) states.

For $E_\alpha = 120$ and 130 MeV α scattering, the reproduction of the 3_1^- cross sections around the second dip ($\theta \approx 15°$) is not satisfactory. This may be explained by higher-order effects that are not considered in the present structure and reaction

calculations; these should be investigated going forward. For example, the in-band $\lambda = 2$ transition of the $3^- $-$5^-$ coupling is omitted in the present calculation. Possible mixing between the $K^\pi = 3_1^-$ and $K^\pi = 0^-$ bands is also expected from the small energy difference in the observed spectra.

For the $1_1^-(K^\pi = 0^-)$ and $1_2^-(K^\pi = 1^-)$ states, no experimental data are available concerning the angular distributions of α-scattering cross sections in this energy range. In the calculated cross sections, a significant state dependence in the CC effects is found between the $1_1^-(K^\pi = 0^-)$ and $1_2^-(K^\pi = 1^-)$ states. The strong CC effects are obtained for the $1_1^-(K^\pi = 0^-)$ cross sections, but not for the $1_2^-(K^\pi = 1^-)$ cross sections; this trend for α scattering is similar to that for p scattering. For the former state $1_1^-(K^\pi = 0^-)$, the strong CC effect arises from the two-step processes via the 3_2^- state, which include the strong $0_1^+ \rightarrow 3_2^-$ ($\lambda = 3$) transition and $3_2^- \rightarrow 1_1^-$ ($\lambda = 2$) transitions. On the other hand, for the latter state $1_2^-(K^\pi = 1^-)$, even though the in-band $\lambda = 2$ transition between the 1_2^- and 3_3^- states is rather strong, the $0_1^+ \rightarrow 3_3^- (\lambda = 3)$ transition is weak. This difference between the $0_1^+ \rightarrow 3_2^-$ and $0_1^+ \rightarrow 3_3^-$ transitions results in different CC effects in the 1_1^- and 1_2^- cross sections, which can be used as an experimental probe for identifying the two dipole modes, provided that the 1^- cross sections are measured. In particular, possible evidence for the 1_1^- state of the $K^\pi = 0^-$ band is the hindered peak amplitude and the dip positions at forward angles of the cross sections, as compared with the 1_2^- cross sections.

V. SUMMARY

The structure and transition properties of the low-lying negative-parity bands of ^{24}Mg were investigated through microscopic structure and reaction calculations via proton and α scattering off ^{24}Mg. In the structure calculation for ^{24}Mg with AMD, the $K^\pi = 0^+$ ground and $K^\pi = 2^+$ sidebands were obtained by triaxial deformation with ^{12}C$+3\alpha$-like (or ^{12}C$+^{12}$C-like) structures. The calculated negative-parity, states were classified into the $K^\pi = 3^-$, $K^\pi = 0^-$, and $K^\pi = 1^-$ bands, which are understood as negative-parity excitations in the deformed system generated by three types of cluster modes. The AMD calculation qualitatively reproduced the observed $E\lambda$-transition strengths and elastic and inelastic charge-form factors.

In the MCC+AMD calculation, the AMD transition densities of ^{24}Mg were renormalized to fit the experimental transition strengths and charge-form factors. Using the renormalized AMD densities, the MCC calculations with the Melbourne g matrix NN interaction were performed for proton and α elastic and inelastic scattering of energies of $E_p = 40$–100 MeV and $E_\alpha = 104$–386 MeV. The MCC+AMD calculations reasonably reproduced the experimental data for proton and α elastic and inelastic cross sections in these energy ranges, except in the case of the 4_1^+ cross sections.

In the reaction analysis of the proton and α inelastic scattering processes using the MCC+AMD calculation, the transition properties of the negative-parity bands were dis-

cussed. Comparison of the calculated (p, p') and (α, α') cross sections as well as the charge form factors with the experimental data showed that the bandhead states of the $K^\pi = 3^-$, $K^\pi = 0^-$, and $K^\pi = 1^-$ bands were assigned to the experimental 3_1^-(7.62 MeV), 1_1^-(7.56 MeV), and 1_2^-(8.44 MeV) states, respectively. Moreover, the 3^- member of the $K^\pi = 0^-$ band was assigned to the 3_2^-(8.36 MeV) state.

The 3_1^- and 3_2^- states were strongly excited by p and α scattering, and one-step processes dominantly contribute to the angular distributions of these cross sections; however, CC effects remain essential for reproducing the absolute amplitudes of the (α, α') cross sections. The shape difference in the $0_1^- \rightarrow 3^-$ transition densities between the 3_1^- and 3_2^- states can be observed in the first-peak shape of the (p, p') and (α, α') cross sections. For 1^- states, the present calculation predicted strong CC effects on the 1_1^- cross sections and weak CC effects on the 1_2^- cross sections. For the 1_1^- cross sections, the strong in-band $\lambda = 2$ transition of the $1_1^- $-$3_2^-$ coupling significantly changes the first-peak shape of the (p, p') cross sections via the two-step process $0_1^+ \rightarrow 3_2^- \rightarrow 1_1^-$, which is supported by proton scattering data. It also strongly affects the 1_1^- cross sections of α scattering.

The present results prove that proton and α inelastic scattering are good probes for investigating the properties of transitions and the band structure of excited states. The MCC approach combining the microscopic structure and reaction calculations was found to be a powerful tool for reaction analysis.

The present AMD calculation is the first microscopic structure calculation to reproduce the energy ordering of the $K^\pi = 0^-$, $K^\pi = 1^-$, and $K^\pi = 3^-$ bands of ^{24}Mg. However, it has problems in precisely reproducing the structural properties. For example, the calculations generally underestimated their transition strengths and overestimated their excitation energies, although it reproduced the energy ordering of the excited bands. These issues remain to be solved by improvement of the structure calculation. The present calculation also failed to reproduce the shape of the $0_1^+ \rightarrow 4_1^+$ form factors, which was a crucial problem for describing the observed (p, p') and (α, α') cross sections for the 4_1^+ state. We can solve this problem with another version of the AMD calculation that yields superior results for the excitation energies and transition properties of the $K^\pi = 0^+$ and $K^\pi = 2^+$ bands. In the next paper [63], we will present a detailed investigation of proton and α inelastic scattering to the 4_1^+ state using the MCC+AMD approach with improved AMD densities for ^{24}Mg.

[1] D. Branford, A. C. McGough, and I. F. Wright, Nucl. Phys. A **241**, 349 (1975).

[2] L. K. Fifield, E. F. Garman, M. J. Hurst, T. J. M. Symons, F. Watt, C. H. Zimmerman, and K. W. Allen, Nucl. Phys. A **322**, 1 (1979).

[3] J. Keinonen, P. Tikkanen, A. Kuronen, Á. Z. Kiss, E. Somorjai, and B. H. Wildenthal, Nucl. Phys. A **493**, 124 (1989).

[4] Y. Horikawa, Y. Torizuka, A. Nakada, S. Mitsunobu, Y. Kojima, and M. Kimura, Phys. Lett. B **36**, 9 (1971).

[5] Y. Horikawa, Prog. Theor. Phys. **47**, 867 (1972).

[6] A. Nakada and Y. Torizuka, J. Phys. Soc. Jpn. **32**, 1 (1972).

[7] A. Johnston and T. E. Drake, J. Phys. A **7**, 898 (1974).

[8] G. C. Li, I. Sick, and M. R. Yearian, Phys. Rev. C **9**, 1861 (1974).

[9] H. Zarek, S. Yen, B. O. Pich, T. E. Drake, C. F. Williamson, S. Kowalski, C. P. Sargent, W. Chung, B. H. Wildenthal, M. Harvey, and H. C. Lee, Phys. Lett. B **80**, 26 (1978).

[10] H. Zarek, S. Yen, B. O. Pich, T. E. Drake, C. F. Williamson, S. Kowalski, and C. P. Sargent, Phys. Rev. C **29**, 1664 (1984).

[11] G. S. Blanpied, J. Hernandez, C. S. Mishra, W. K. Mize, C. S. Whisnant, B. G. Ritchie, C. L. Morris, S. J. Seestrom-Morris, C. F. Moore, P. A. Seidl, R. A. Lindgren, B. H. Wildenthal, and R. Gilman, Phys. Rev. C **41**, 1625 (1990).

[12] G. Haouat, C. Lagrange, R. de Swiniarski, F. Dietrich, J. P. Delaroche, and Y. Patin, Phys. Rev. C **30**, 1795 (1984).

[13] A. A. Rush, E. J. Burge, V. E. Lewis, D. A. Smith, and N. K. Ganguly, Nucl. Phys. A **104**, 340 (1967).

[14] A. A. Rush and N. K. Ganguly, Nucl. Phys. A **117**, 101 (1968).

[15] B. Zwieglinski, G. M. Crawley, H. Nann, and J. A. Nolen, Phys. Rev. C **17**, 872 (1978).

[16] B. Zwieglinski, G. M. Crawley, W. Chung, H. Nann, and J. A. Nolen, Phys. Rev. C **18**, 1228 (1978).

[17] S. Kato, K. Okada, M. Kondo, K. Hosono, T. Saito, N. Matsuoka, K. Hatanaka, T. Noro, S. Nagamachi, H. Shimizu, K. Ogino, Y. Kadota, S. Matsuki, and M. Wakai, Phys. Rev. C **31**, 1616 (1985).

[18] Y. S. Horowitz, N. K. Sherman, and R. E. Bell, Nucl. Phys. A **134**, 577 (1969).

[19] R. M. Lombard, J. L. Escudie, and M. Soyeur, Phys. Rev. C **18**, 42 (1978).

[20] L. Ray, G. S. Blanpied, and W. R. Coker, Phys. Rev. C **20**, 1236 (1979).

[21] G. Blanpied, N. M. Hintz, G. S. Kyle, J. W. Palm, R. Liljestrand, M. Barlett, C. Harvey, G. W. Hoffmann, L. Ray, and D. G. Madland, Phys. Rev. C **20**, 1490 (1979).

[22] R. De Leo, G. D'Erasmo, A. Pantaleo, M. N. Harakeh, S. Micheletti, and M. Pignanelli, Phys. Rev. C **23**, 1355 (1981).

[23] K. Amos and W. Bauhoff, Nucl. Phys. A **424**, 60 (1984).

[24] R. J. Griffiths, Nucl. Phys. A **102**, 329 (1967).

[25] K. Van Der Borg, M. N. Harakeh, and B. S. Nilsson, Nucl. Phys. A **325**, 31 (1979).

[26] I. M. Naqib and J. S. Blair, Phys. Rev. **165**, 1250 (1968).

[27] H. Rebel, G. W. Schweimer, G. Schatz, J. Specht, R. Löhken, G. Hauser, D. Habs, and H. Klewe-Nebenius, Nucl. Phys. A **182**, 145 (1972).

[28] K. Van Der Borg, M. N. Harakeh, and A. Van Der Woude, Nucl. Phys. A **365**, 243 (1981).

[29] S. Adachi, T. Kawabata, K. Minomo, T. Kadoya, N. Yokota, H. Akimune, T. Baba, H. Fujimura, M. Fujiwara, Y. Funaki, T. Furuno, T. Hashimoto, K. Hatanaka, K. Inaba, Y. Ishii, M. Itoh, C. Iwamoto, K. Kawase, Y. Maeda, H. Matsubara, Y. Matsuda, H. Matsuno, T. Morimoto, H. Morita, M. Murata, T. Nanamura, I. Ou, S. Sakaguchi, Y. Sasamoto, R. Sawada, Y. Shimizu, K. Suda, A. Tamii, Y. Tameshige, M. Tsumura, M. Uchida, T. Uesaka, H. P. Yoshida, and S. Yoshida, Phys. Rev. C **97**, 014601 (2018).

[30] V. O. Nesterenko, A. Repko, J. Kvasil, and P. G. Reinhard, Phys. Rev. Lett. **120**, 182501 (2018).

[31] V. O. Nesterenko, A. Repko, J. Kvasil, and P. G. Reinhard, Phys. Rev. C **100**, 064302 (2019).

[32] M. Kimura, R. Yoshida, and M. Isaka, Prog. Theor. Phys. **127**, 287 (2012).

[33] Y. Chiba, Y. Kanada-En'yo, and Y. Shikata, arXiv:1911.08734 [nucl-th].

[34] Y. Kanada-Enyo and H. Horiuchi, Prog. Theor. Phys. **93**, 115 (1995).

[35] Y. Kanada-En'yo, H. Horiuchi, and A. Ono, Phys. Rev. C **52**, 628 (1995).

[36] Y. Kanada-En'yo, Phys. Rev. Lett. **81**, 5291 (1998).

[37] Y. Kanada-En'yo, M. Kimura, and A. Ono, Prog. Theor. Exp. Phys. **2012**, 01A202 (2012).

[38] Y. Kanada-En'yo and K. Ogata, Phys. Rev. C **99**, 064601 (2019).

[39] Y. Kanada-En'yo and K. Ogata, Phys. Rev. C **99**, 064608 (2019).

[40] Y. Kanada-En'yo and K. Ogata, Phys. Rev. C **100**, 064616 (2019).

[41] Y. Kanada-En'yo and K. Ogata, Phys. Rev. C **101**, 064607 (2020).

[42] Y. Kanada-En'yo and K. Ogata, Phys. Rev. C **101**, 064308 (2020).

[43] K. Ogata, Y. Chiba, and Y. Sakuragi, arXiv:2001.09627 [nucl-th].

[44] K. Amos, P. J. Dortmans, H. V. von Geramb, S. Karataglidis, and J. Raynnal, in *Advances in Nuclear Physics*, edited by J. W. Negele and E. Vogt, Part of the Advances in Nuclear Physics Book Series, Vol. 25 (Springer, Boston, MA, 2002), pp. 276–536.

[45] Y. Kanada-En'yo, H. Horiuchi, and A. Dote, Phys. Rev. C **60**, 064304 (1999).

[46] Y. Kanada-En'yo and H. Horiuchi, Phys. Rev. C **68**, 014319 (2003).

[47] T. Ando, K. Ikeda, and A. Tohsaki, Prog. Theor. Phys. **64**, 1608 (1980).

[48] R. Tamagaki, Prog. Theor. Phys. **39**, 91 (1968).

[49] N. Yamaguchi, T. Kasahara, S. Nagata, and Y. Akaishi, Prog. Theor. Phys. **62**, 1018 (1979).

[50] K. Minomo, K. Ogata, M. Kohno, Y. R. Shimizu, and M. Yahiro, J. Phys. G **37**, 085011 (2010).

[51] F. A. Brieva and J. R. Rook, Nucl. Phys. A **291**, 299 (1977).

[52] F. A. Brieva and J. R. Rook, Nucl. Phys. A **291**, 317 (1977).

[53] F. A. Brieva and J. R. Rook, Nucl. Phys. A **297**, 206 (1978).

[54] W. Haider, Syed Rafi, J. R. Rook, and Y. K. Gambhir, Phys. Rev. C **93**, 054615 (2016).

[55] K. Hagino, T. Takehi, and N. Takigawa, Phys. Rev. C **74**, 037601 (2006).

[56] M. Toyokawa, K. Minomo, and M. Yahiro, Phys. Rev. C **88**, 054602 (2013).

[57] M. Toyokawa, M. Yahiro, T. Matsumoto, K. Minomo, K. Ogata, and M. Kohno, Phys. Rev. C **92**, 024618 (2015); **96**, 059905(E) (2017).

[58] K. Minomo, K. Washiyama, and K. Ogata, arXiv:1712.10121 [nucl-th].

[59] K. Egashira, K. Minomo, M. Toyokawa, T. Matsumoto, and M. Yahiro, Phys. Rev. C **89**, 064611 (2014).

[60] R. Machleidt, K. Holinde, and Ch. Elster, Phys. Reports **149**, 1 (1987).

[61] K. Minomo and K. Ogata, Phys. Rev. C **93**, 051601(R) (2016).

[62] R. B. Firestone, Nucl. Data Sheets **108**, 2319 (2007).

[63] Y. Kanada-En'yo and K. Ogata, arXiv:2010.08150 [nucl-th].

[64] I. Angeli and K. P. Marinova, At. Data Nucl. Data Tables **99**, 69 (2013).

[65] T. Kibédi and R. h. Spear, Atom. Data Nucl. Data Tabl. **80**, 35 (2002).

[66] B. A. Brown, W. Chung, and B. H. Wildenthal, Phys. Rev. C **21**, 2600 (1980).

[67] M. Carchidi, B. H. Wildenthal, and B. A. Brown, Phys. Rev. C **34**, 2280 (1986).

[68] B. A. Brown and B. H. Wildenthal, Ann. Rev. Nucl. Part. Sci. **38**, 29 (1988).

[69] Y. Utsuno, T. Otsuka, and H. Nakada, Phys. Lett. B **397**, 6 (1997).

[70] N. Otuka, E. Dupont, V. Semkova, B. Pritychenko, A. I. Blokhin, M. Aikawa, S. Babykina, M. Bossant, G. Chen, S. Dunaeva, R. A. Forrest, T. Fukahori, N. Furutachi, S. Ganesan, Z. Ge, O. O. Gritzay, M. Herman, S. Hlavač, K. Katō, B. Lalremruata, Y. O. Lee, A. Makinaga, K. Matsumoto, M. Mikhaylyukova, G. Pikulina, V. G. Pronyaev, A. Saxena, O. Schwerer, S. P. Simakov, N. Soppera, R. Suzuki, S. Takács, X. Tao, S. Taova, F. Tárkányi, V. V. Varlamov, J. Wang, S. C. Yang, V. Zerkin, and Y. Zhuang, Nucl. Data Sheets **120**, 272 (2014).